

Finite-Element Analysis of Ceramic Multilayer Capacitors: Failure Probability Caused by Wave Soldering and Bending Loads

Klaus Franken and Horst R. Maier

Institut für Keramische Komponenten im Maschinenbau, RWTH Aachen, 52056 Aachen, Germany

Klaus Prume and Rainer Waser^{*,†}

Institut für Werkstoffe der Elektrotechnik, RWTH Aachen, 52056 Aachen, Germany

A two-dimensional numerical model that predicts the reliability of multilayer capacitors (MLCs) during soldering and bending is presented. The Weibull parameters used in the model are based on measurements of soldered MLC devices. The preheating and soldering temperatures have a dominant impact on the failure probability, in comparison to the thickness of the nickel layer, the soft solder geometry, and the number of inner electrodes. Comparison of calculated and measured reliability of three MLC sizes leads to the assumption that residual stresses due to the manufacturing process or size-related microstructure are important.

I. Introduction

CERAMIC multilayer capacitors (MLCs) are used in most surface-mounted circuits for many applications, such as telecommunications, automotive engineering, or aeronautics. Because of the high safety demand of electronic systems and the large sum of integrated parts, the required high reliability of each MLC is evident.^{1,2} The components mainly are stressed by mechanical, thermal, and electrical loads, which create coupled reactions. Investigation of these effects, using finite element modeling (FEM), has been conducted in close cooperation between the Institut für Werkstoffe der Elektrotechnik (IWE) and the Institut für Keramische Komponenten im Maschinenbau (IKKM) and will lead to a series of papers.

This paper examines some aspects of the mechanical and thermal loads of MLCs. A typical thermal load is the thermal shock created by wave soldering.^{3,4} Mechanical loading occurs during component integration or circuit operation in the form of board bending.⁵ Cracks that change the mechanical and, especially, the electrical performance of MLCs may result from this loading. Three different component sizes (1206, 1210, and 1812; the first two digits of these four-digit size numbers indicate the component length, the last two digits is the component width, given in increments of 0.01 in.) are investigated in this paper; each component is composed of a BaTiO₃-based dielectric with a Type X7R temperature characteristic, sintered at high temperature. Measurements and calculations are performed to investigate the component behavior, for the purpose of predicting the component failure probability during typical wave soldering processes, after soldering and cooling to room temperature, and during the bending

of soldered MLC devices. The initial state of the simulation is assumed to be stress free, which means that stresses due to the manufacturing process are not considered yet. Up to this point in time, numerical simulations made for MLCs most often have been evaluated by evaluating the calculated stresses or stress gradients. First, calculations to predict the failure probability of MLCs were presented.⁶ A numerical postprocessor for reliability analysis is used at IKKM.^{7,8} The processor that works with Weibull's theory needs the input of stress fields and the Weibull parameters. Stress fields are calculated via FEM, and the Weibull parameters are derived using measurements and a numerical evaluation of the measured results. A confidence estimation of the derived parameters is given.

A parametrical study that includes the variation of soldering temperature, the preheating temperature, the thickness of the nickel layer, the number of inner electrodes, and the soft solder geometry is performed for the 1206 size. The failure probability is calculated for each parameter from preheating to bending, and the results are discussed and compared to the findings of other authors.

II. Experimental Procedure

Four-point bending measurements of soldered MLC devices were performed to improve the numerical model and to obtain the required material data for probability analyses. Contrary to the flex test,⁹ which is a three-point bending test, the influence of the test-jig radius is almost eliminated in the four-point bending test. The principles of the measurement facility are shown in Fig. 1. The width (b) of the printed circuit board (PCB) was chosen to be identical to that of the applied MLC. The following FEM simulations were performed with a two-dimensional model that assumed the same width of all modeled parts. The MLCs were soldered to the board very carefully by hand, to prevent thermal shock. The solder type was L-Sn60PbCu2/zh, with 2.5% flux, soldered at 250°C. The soldered devices were loaded in a testing machine (Instron, Danvers, MA) with a load rate of 1 mm/s. Fracture was detected by observing the load-time history. The total stiffness of the soldered device decreases in the case of MLC fracture, as does the load. Therefore, the first significant decrease in load was interpreted to be the fracture load (F_f). Microscopic analysis of the tested MLCs ensured that the observed decrease in force could be allocated to a crack. Three different MLC sizes—1206, 1210, and 1812—were tested. The MLCs were comprised of BaTiO₃-based dielectrics, according to the Electronics Industry Association (EIA) specification X7R (maximum change in permittivity of $\pm 15\%$ in the temperature range from -55°C to $+125^\circ\text{C}$), and were sintered at 1320°C . The inner electrodes were composed of $\sim 30\%$ silver and 70% palladium; the termination was made of layered silver, nickel, and tin. The different MLC sizes and the number of tested specimens are shown in Table I. The measured typical thickness of the inner electrodes was $\sim 2.5\ \mu\text{m}$, and the thickness of the PCB was 1.6 mm.

A. Jagota—contributing editor

Manuscript No. 189950. Received August 17, 1998; approved November 11, 1999. Supported by the Deutsche Forschungsgemeinschaft (German Research Society), Bonn, Germany.

^{*}Member, American Ceramic Society.

[†]Also with Institut für Festkörperforschung, Forschungszentrum Jülich, 52425 Jülich, Germany.

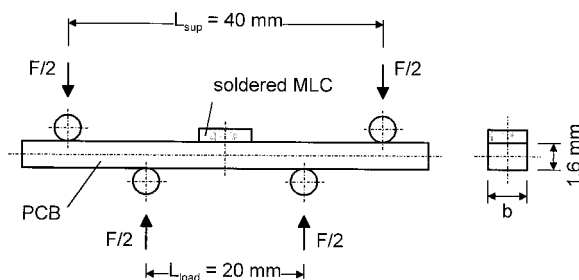


Fig. 1. Principle of the four-point bending facility. (Loading rate of 1 mm/s.)

Table I. Data Regarding the Tested MLCs

Component size [†]	Number of active layers	Component thickness (mm)	Number of specimens
1206	12	1.03	26
1210	4	0.84	30
1812	4	0.75	24

[†]Each sample is Type X7R. First two digits indicate the component length, and the last two digits represent the component width in increments of 0.01 in.

A typical test result is depicted in Fig. 2, which shows a polished cross section of a cracked MLC. The crack runs from the end of the termination (board side) into the termination, cutting off most of the inner electrodes. The fracture moment ($M_{f,i}$) is calculated for each specimen i from the measured fracture loads $F_{f,i}$ and the test geometry using Eq. (1),

$$M_{f,i} = \frac{F_{f,i}}{4} (L_{\text{sup}} - L_{\text{load}}) \quad (1)$$

where L_{sup} denotes the support span and L_{load} the load span (see Fig. 1). The fracture probability (P_f , which is equal to $i/(n+1)$, where n represents the total number of specimens in one series) versus $M_{f,i}$ is plotted in Fig. 3. The $M_{f,i}$ values are in the range of ~ 0.15 – 0.4 N·m. The Weibull parameters are determined after converting the fracture moments to fracture stresses (see section III(3)).

III. Numerical Procedure

(1) Model Description

The two-dimensional numerical model used for this simulation was created using the ANSYS[®] FEM software¹⁰ and contains plane-stress elements. Only half of the cross-sectional area of a soldered MLC is modeled, without any loss of accuracy; the model

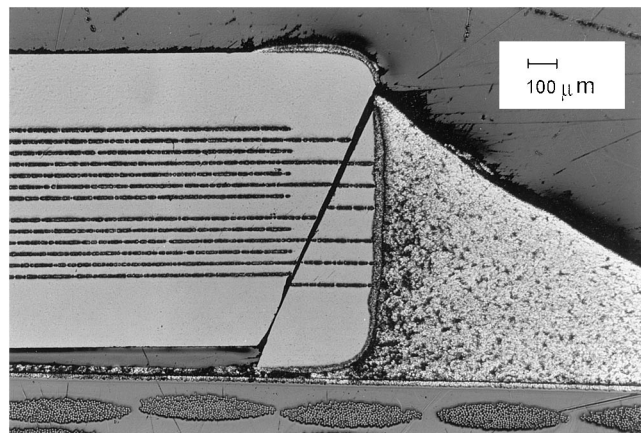


Fig. 2. Polished cross section of a typical crack through a soldered MLC due to an external bending moment.

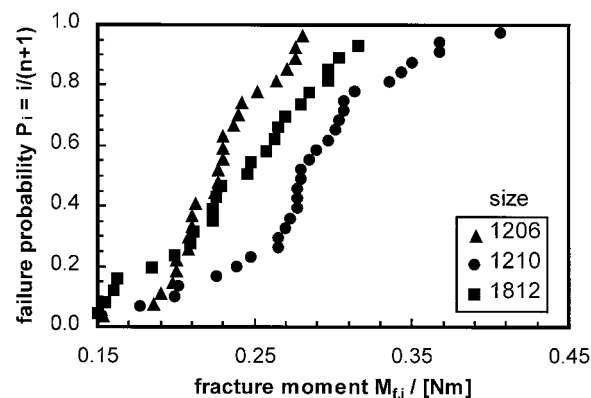


Fig. 3. Measured fracture moments of four-point bending test of soldered Type X7R MLC sizes.

is depicted in Fig. 4. The total inner and outer geometry of the MLC, including the inner electrodes and the termination, as well as the soft solder geometry, the copper cladding layer of the PCB, and the PCB itself, are considered. The individual finite elements are not shown in Fig. 4, because of their large population (typically $\sim 12\,000$). The electrodes are modeled with three elements in thickness and define the resolution of the remaining model, with a limited aspect ratio. The geometry of the model was obtained from polished sections of soldered devices.

Generally, the model is suitable for the calculation of thermal, mechanical, and electrical load cases. In this study, the calculations are reduced to mechanical and thermal loads and results. The temperatures are calculated transiently, so that time-dependent effects such as thermal shock can be investigated. A stress distribution has been derived for each temperature distribution, which leads to a stress history that can be evaluated in further steps.

The material properties, relative to the temperature of all materials involved, are required for the simulation. Sufficient temperature-dependent material data are available in the literature for BaTiO₃, nickel, tin, silver, palladium, PbSn soft solder, epoxy, and copper.^{11–17} Except for the coefficients of thermal expansion (α),¹⁸ data for a specific silver/palladium alloy were difficult to find. Therefore, most of its material properties were derived by interpolating the values of pure silver and palladium with uncertain accuracy. The deformation behavior of the dielectric and the board was assumed to be elastic; the metals could undergo plastic

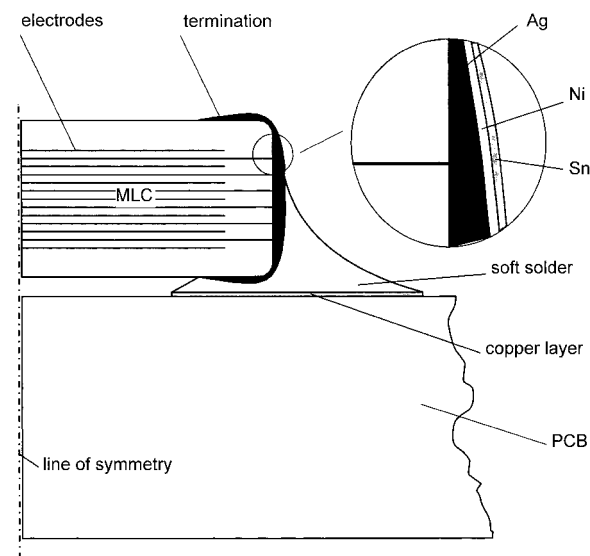


Fig. 4. Typical shape of a numerical (FEM) model of a soldered MLC. (Finite-element mesh not shown.)

Table II. Properties of the Internal Electrodes at Various Temperatures[†]

Property	Value [‡]			
	RT	100°C	200°C	300°C
Elastic modulus, E	110 GPa	108 GPa	106 GPa	104 GPa
Poisson's ratio, ν	0.35	0.35	0.35	0.35
Density, ρ	11561 kg/m ³	11471 kg/m ³	11358 kg/m ³	11246 kg/m ³
Yield strength, $R_{p,0.2}$	74 MPa	74 MPa	73 MPa	66 MPa
Coefficient of thermal expansion, α	$11.01 \times 10^{-6} \text{ K}^{-1}$	$11.13 \times 10^{-6} \text{ K}^{-1}$	$11.28 \times 10^{-6} \text{ K}^{-1}$	$12.00 \times 10^{-6} \text{ K}^{-1}$
Thermal conductivity, k	$178 \text{ W} \cdot (\text{m} \cdot \text{K})^{-1}$	$177 \text{ W} \cdot (\text{m} \cdot \text{K})^{-1}$	$175 \text{ W} \cdot (\text{m} \cdot \text{K})^{-1}$	$173 \text{ W} \cdot (\text{m} \cdot \text{K})^{-1}$
Specific heat, C_p	$242 \text{ J} \cdot (\text{kg} \cdot \text{K})^{-1}$	$246 \text{ J} \cdot (\text{kg} \cdot \text{K})^{-1}$	$250 \text{ J} \cdot (\text{kg} \cdot \text{K})^{-1}$	$256 \text{ J} \cdot (\text{kg} \cdot \text{K})^{-1}$

[†]Property values are based on a 30% silver–70% palladium internal electrode composition. [‡]Data for α are from Touloukian;¹⁸ all other data have been linearly extrapolated from data for silver and palladium.

Table III. Properties of the BaTiO₃-Based X7R Dielectric at Various Temperatures

Property	Value						
	RT	50°C	100°C	120°C	150°C	200°C	300°C
Elastic modulus, E^{\dagger}	91 GPa		108 GPa		175 GPa		
Poisson's ratio, ν^{\ddagger}	0.33	0.33	0.33	0.33	0.33	0.33	0.33
Density, ρ^{\ddagger}	6000 kg/m ³	6000 kg/m ³	6000 kg/m ³	6000 kg/m ³	6000 kg/m ³	6000 kg/m ³	6000 kg/m ³
Coefficient of thermal expansion, α^{\S}	$7.6 \times 10^{-6} \text{ K}^{-1}$	$8.0 \times 10^{-6} \text{ K}^{-1}$	$8.2 \times 10^{-6} \text{ K}^{-1}$	$8.2 \times 10^{-6} \text{ K}^{-1}$	$7.8 \times 10^{-6} \text{ K}^{-1}$	$8.6 \times 10^{-6} \text{ K}^{-1}$	$9.8 \times 10^{-6} \text{ K}^{-1}$
Thermal conductivity, k^{\ddagger}	$5 \text{ W} \cdot (\text{m} \cdot \text{K})^{-1}$	$5 \text{ W} \cdot (\text{m} \cdot \text{K})^{-1}$	$5 \text{ W} \cdot (\text{m} \cdot \text{K})^{-1}$	$5 \text{ W} \cdot (\text{m} \cdot \text{K})^{-1}$	$5 \text{ W} \cdot (\text{m} \cdot \text{K})^{-1}$	$5 \text{ W} \cdot (\text{m} \cdot \text{K})^{-1}$	$5 \text{ W} \cdot (\text{m} \cdot \text{K})^{-1}$
Specific heat, C_p^{\ddagger}	$502 \text{ J} \cdot (\text{kg} \cdot \text{K})^{-1}$	$502 \text{ J} \cdot (\text{kg} \cdot \text{K})^{-1}$	$502 \text{ J} \cdot (\text{kg} \cdot \text{K})^{-1}$	$502 \text{ J} \cdot (\text{kg} \cdot \text{K})^{-1}$	$502 \text{ J} \cdot (\text{kg} \cdot \text{K})^{-1}$	$502 \text{ J} \cdot (\text{kg} \cdot \text{K})^{-1}$	$502 \text{ J} \cdot (\text{kg} \cdot \text{K})^{-1}$

[†]From Duffy *et al.*¹¹ Values were determined using linear extrapolation. [‡]From Scott and Astfalk.¹² [§]By IKKM.

Table IV. Properties for Layered Termination (Silver, Nickel, and Tin)

Property	Value				Reference
	RT	100°C	200°C	300°C	
Layer 1, Silver					
Elastic modulus, E	81.8 GPa	75.6 GPa	74.8 GPa	70.3 GPa	Stelzer ¹³
Poisson's ratio, ν	0.35	0.35	0.35	0.35	Scott and Astfalk ¹²
Density, ρ	10490 kg/m ³	10389 kg/m ³	10262 kg/m ³	10136 kg/m ³	Reference 14
Yield strength, $R_{p,0.2}$	35.4 MPa	30.6 MPa	24.5 MPa	18.2 MPa	Stelzer ¹³
Coefficient of thermal expansion, α	$17.8 \times 10^{-6} \text{ K}^{-1}$	$18.2 \times 10^{-6} \text{ K}^{-1}$	$18.8 \times 10^{-6} \text{ K}^{-1}$	$19.3 \times 10^{-6} \text{ K}^{-1}$	Stelzer ¹³
Thermal conductivity, k	$423 \text{ W}\cdot(\text{m}\cdot\text{K})^{-1}$	$415 \text{ W}\cdot(\text{m}\cdot\text{K})^{-1}$	$399 \text{ W}\cdot(\text{m}\cdot\text{K})^{-1}$	$383 \text{ W}\cdot(\text{m}\cdot\text{K})^{-1}$	Stelzer ¹³
Specific heat, C_p	$233 \text{ J}\cdot(\text{kg}\cdot\text{K})^{-1}$	$237 \text{ J}\cdot(\text{kg}\cdot\text{K})^{-1}$	$242 \text{ J}\cdot(\text{kg}\cdot\text{K})^{-1}$	$248 \text{ J}\cdot(\text{kg}\cdot\text{K})^{-1}$	Stelzer ¹³
Layer 2, nickel					
Elastic modulus, E	207 GPa	205 GPa	203 GPa	200 GPa	Stelzer ¹³
Poisson's ratio, ν	0.31	0.31	0.31	0.31	Reference 14
Density, ρ	8902 kg/m ³	8902 kg/m ³	8902 kg/m ³	8902 kg/m ³	Reference 14
Yield strength, $R_{p,0.2}$	148 MPa	155 MPa	145 MPa	143 MPa	Stelzer ¹³
Coefficient of thermal expansion, α	$13.3 \times 10^{-6} \text{ K}^{-1}$	$13.5 \times 10^{-6} \text{ K}^{-1}$	$13.8 \times 10^{-6} \text{ K}^{-1}$	$14.1 \times 10^{-6} \text{ K}^{-1}$	Reference 14
Thermal conductivity, k	$67 \text{ W}\cdot(\text{m}\cdot\text{K})^{-1}$	$60 \text{ W}\cdot(\text{m}\cdot\text{K})^{-1}$	$52 \text{ W}\cdot(\text{m}\cdot\text{K})^{-1}$	$47 \text{ W}\cdot(\text{m}\cdot\text{K})^{-1}$	Stelzer ¹³
Specific heat, C_p	$430 \text{ J}\cdot(\text{kg}\cdot\text{K})^{-1}$	$475 \text{ J}\cdot(\text{kg}\cdot\text{K})^{-1}$	$532 \text{ J}\cdot(\text{kg}\cdot\text{K})^{-1}$	$589 \text{ J}\cdot(\text{kg}\cdot\text{K})^{-1}$	Stelzer ¹³
Layer 3, tin					
Elastic modulus, E	54.0 GPa	48.4 GPa	35.5 GPa		Stelzer ¹³
Poisson's ratio, ν	0.33	0.33	0.33		Reference 14
Density, ρ	7168 kg/m ³	7168 kg/m ³	7168 kg/m ³		Reference 14
Yield strength, $R_{p,0.2}$	14.5 MPa	11.0 MPa	4.5 MPa		Reference 15
Coefficient of thermal expansion, α	$25.6 \times 10^{-6} \text{ K}^{-1}$	$30.0 \times 10^{-6} \text{ K}^{-1}$	$38.9 \times 10^{-6} \text{ K}^{-1}$		Stelzer ¹³
Thermal conductivity, k	$66.5 \text{ W}\cdot(\text{m}\cdot\text{K})^{-1}$	$63.3 \text{ W}\cdot(\text{m}\cdot\text{K})^{-1}$	$60.2 \text{ W}\cdot(\text{m}\cdot\text{K})^{-1}$		Stelzer ¹³
Specific heat, C_p	$221 \text{ J}\cdot(\text{kg}\cdot\text{K})^{-1}$	$232 \text{ J}\cdot(\text{kg}\cdot\text{K})^{-1}$	$253 \text{ J}\cdot(\text{kg}\cdot\text{K})^{-1}$		Stelzer ¹³

deformation, which was described by a bilinear kinematic hardening law. The parameters are the temperature-dependent yield stress and the tangent modulus, which is fixed at 10% of the temperature-dependent elastic modulus, in accordance with FEM practices. Time-dependent deformation (creep) is neglected. The material data used for the simulations are summarized in Tables II–VII.

(2) Statistical Analysis

Effects of failure probability can be described by the Weibull theory, based on the weakest-link model.^{19,20} The distribution of volume and/or surface flaws can be investigated. The failure probability for dominant volume flaws ($F_V(\sigma)$) is dependent on the

tensile-stress distribution ($\sigma(x,y,z)$), the Weibull modulus for volume flaws (m_V), and the characteristic strength (σ_{OV}):

$$F_V(\sigma) = 1 - \exp \left[- \frac{1}{V_0} \int_V \left(\frac{\sigma(x,y,z)}{\sigma_{OV}} \right)^{m_V} dV \right] \quad (2)$$

The tensile-stress distribution also can be written as

$$\sigma(x, y, z) = \sigma_p f(x,y,z) \quad (3)$$

where σ_p denotes a predestined stress (e.g., the maximum tensile stress) and $f(x,y,z)$ is the stress function. The characteristic strength

Table V. Properties of the Copper Cladding

Property	Value				Reference
	RT	100°C	200°C	300°C	
Elastic modulus, E	131 GPa	127 GPa	121 GPa	116 GPa	Stelzer ¹³
Poisson's ratio, ν	0.308	0.308	0.308	0.308	Reference 14
Density, ρ	8930 kg/m ³	8856 kg/m ³	8763 kg/m ³	8670 kg/m ³	Reference 14
Yield strength, $R_{p,0.2}$	57 MPa	54 MPa	50 MPa	45 MPa	Stelzer ¹³
Coefficient of thermal expansion, α	$16.7 \times 10^{-6} \text{ K}^{-1}$	$17.4 \times 10^{-6} \text{ K}^{-1}$	$18.2 \times 10^{-6} \text{ K}^{-1}$	$19.1 \times 10^{-6} \text{ K}^{-1}$	Stelzer ¹³
Thermal conductivity, k	$407 \text{ W} \cdot (\text{m} \cdot \text{K})^{-1}$	$394 \text{ W} \cdot (\text{m} \cdot \text{K})^{-1}$	$381 \text{ W} \cdot (\text{m} \cdot \text{K})^{-1}$	$371 \text{ W} \cdot (\text{m} \cdot \text{K})^{-1}$	Stelzer ¹³
Specific heat, C_p	$387 \text{ J} \cdot (\text{kg} \cdot \text{K})^{-1}$	$396 \text{ J} \cdot (\text{kg} \cdot \text{K})^{-1}$	$408 \text{ J} \cdot (\text{kg} \cdot \text{K})^{-1}$	$420 \text{ J} \cdot (\text{kg} \cdot \text{K})^{-1}$	Stelzer ¹³

Table VI. Properties of the Epoxy Board[†]

Property	Value	Measurement temperature (°C)
Elastic modulus, E	23 GPa	RT
Poisson's ratio, ν	0.25	RT
Density, ρ	1800 kg/m ³	154.4
Coefficient of thermal expansion, α	$14.4 \times 10^{-6} \text{ K}^{-1}$	RT–125
Thermal conductivity, k	$0.5 \text{ W} \cdot (\text{m} \cdot \text{K})^{-1}$	RT
Specific heat, C_p	$1465 \text{ J} \cdot (\text{kg} \cdot \text{K})^{-1}$	RT

[†]All measurements except the elastic modulus were taken from Scott and Astfalk;¹² the E value was measured by IKKM.

is defined as the uniaxial tensile stress in a volume of 1 mm³ (V_0) at a failure probability of 63.2%. By logarithmizing Eq. (2) twice and introducing a so-called effective volume (V_{eff}),

$$V_{\text{eff}} = \int_V (f(x, y, z))^{m_V} dV \quad (4)$$

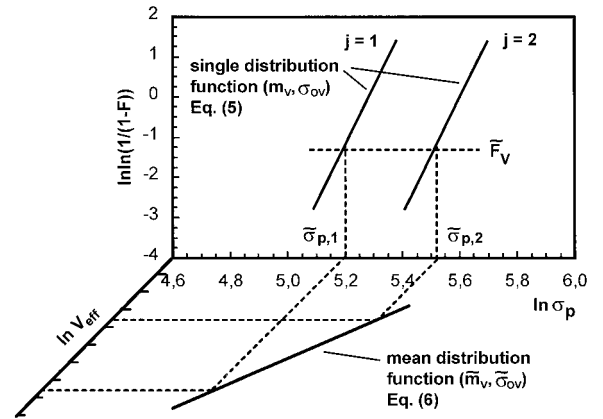
a distribution function for a single measurement series can be derived:

$$\ln \ln \left(\frac{1}{1 - F_V} \right) = m_V \ln \sigma_p - m_V \ln \sigma_{OV} + \ln \left(\frac{V_{\text{eff}}}{V_0} \right) \quad (5)$$

Ranking the single-measurement stresses $\sigma_{p,i}$ in increasing order and assuming a fracture probability $P_i = i/(n+1)$ for each single measurement i of a series with n specimens, Eq. (5) can be fitted (e.g., by the maximum likelihood method) to the plot $P_i(\sigma_{p,i})$ and leads to the Weibull parameters $(m_V, \sigma_{OV})_j$ for the single-distribution function. Comparison of different measurement series j at a common failure probability of $\bar{F}_V = \text{constant}$ (e.g., 63.2%) gives the corresponding mean distribution function:

$$\ln \sigma_{p,j} = -\frac{1}{m_V} \ln \left(\frac{V_{\text{eff},j}}{V_0} \right) + \ln \sigma_{OV} + \frac{1}{m_V} \ln \ln \left(\frac{1}{1 - F_V} \right) \quad (6)$$

Fitting Eq. (6) to the $\sigma_{p,j}(V_{\text{eff},j})$ plot (e.g., by the least-squares method) leads to the Weibull parameters $(\bar{m}_V, \bar{\sigma}_{OV})$ for the

**Fig. 5.** Single-distribution and mean-distribution functions.

mean-distribution function. The correlation between the single-distribution and the mean-distribution function is illustrated in Fig. 5.

Special attention must be given to the elements, with declining stresses versus time, when applying Eqs. (2)–(6) to stress histories of each volume element k . The overall failure probability ($F_{V,\text{all}}$) at an evaluation time t_e is a result of the maximum failure probability ($F_{V,\text{max}}$) of each volume element within the interval of t_0 to t_e . The principle of independent action (PIA) is used, relative to the principal stresses $\sigma_{k,z}$ within each volume element and for the superposition of all volume elements N :

$$(F_{V,\text{max}})_{k,z} = \max(F_V)_{k,z|t_0=t_e} \quad (7)$$

$$1 - F_{V,\text{all}} = \prod_{z=1}^3 \left[\prod_{k=1}^N (1 - (F_{V,\text{max}})_{k,z}) \right] \quad (8)$$

A corresponding postprocessor routine that can read the output of the FEM simulation has been established.

(3) Statistical Evaluation of Bending Tests

Figure 3 shows the Weibull plots of the fracture probability P_i versus the fracture moment $M_{f,i}$ for the three MLC sizes that have

Table VII. Properties of the Soft Solder (Sn63/Pb37)

Property	Value [†]			Reference
	0°C	50°C	100°C	
Elastic modulus, E	26.5 GPa	12.5 GPa	2.9 GPa	Cole and Caulfield ¹⁶
Poisson's ratio, ν	0.36	0.36	0.36	Magomedov ¹⁷
Density, ρ	8420 kg/m ³	8420 kg/m ³	8420 kg/m ³	Reference 14
Yield strength, $R_{p,0.2}$	36.4 MPa	15.2 MPa	5.8 MPa	Cole and Caulfield ¹⁶
Coefficient of thermal expansion, α	$24.7 \times 10^{-6} \text{ K}^{-1}$	$24.7 \times 10^{-6} \text{ K}^{-1}$	$24.7 \times 10^{-6} \text{ K}^{-1}$	Reference 14
Thermal conductivity, k	$50 \text{ W} \cdot (\text{m} \cdot \text{K})^{-1}$	$50 \text{ W} \cdot (\text{m} \cdot \text{K})^{-1}$	$50 \text{ W} \cdot (\text{m} \cdot \text{K})^{-1}$	Reference 14
Specific heat, C_p	$176 \text{ J} \cdot (\text{kg} \cdot \text{K})^{-1}$	$176 \text{ J} \cdot (\text{kg} \cdot \text{K})^{-1}$	$176 \text{ J} \cdot (\text{kg} \cdot \text{K})^{-1}$	Reference 15

[†]Data for ν and ρ were obtained at room temperature. Data for α were obtained over a temperature range of 15°–110°C. Data for λ were obtained over a temperature range of 0°–180°C. Data for C_p were obtained for Sn60Pb at room temperature.

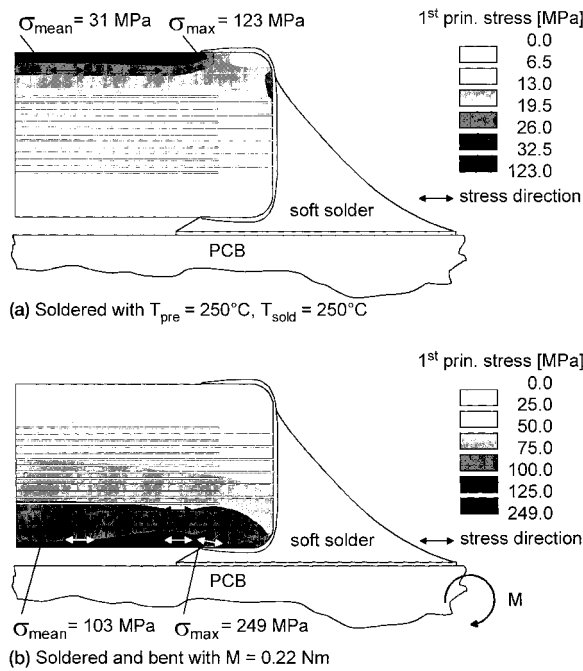


Fig. 6. Calculated distribution of first principal stress in the dielectric of a MLC (a) at room temperature (preheated at 250°C, soldered at 250°C) and (b) soldered and bent ($M = 0.22$ N·m).

been tested according to Fig. 1. To derive the Weibull parameters, the $M_{f,i}$ values were translated to predestined stresses $\sigma_{p,i}$ as follows. The stress fields at the fracture point of the MLCs principally include (i) residual stresses due to manufacturing, (ii) joining stresses due to soldering, and (iii) load stresses due to bending.

First, residual-stress measurements (using X-ray diffractometry (XRD)) at the component surface show in-plane compressive stresses up to 60 MPa. The total residual-stress distribution is not yet known; therefore, residual stresses at room temperature are not considered.

The joining stresses at room temperature after cooling from the soldering temperature are simulated using FEM analysis. The calculations are performed as described in section III(4), using a thermal-shock-free preheating to the soldering temperature of 250°C. The soldering process of the tested specimen was conducted accordingly. The joining-stress profile at room temperature

shows tensile stresses in the cover layer of the free MLC side (top side) and compressive stresses in the lower cover layer (see Fig. 6(a)). The tensile-stress direction is parallel to the electrodes and attains the maximum value near the termination edge.

Load stresses that are due to bending of the soldered device lead to tensile stresses in the lower layer (PCB side) and compressive stresses in the upper component cover layer. These compressive stresses compensate the tensile joining stresses in the upper cover layer. The distribution of the first principal stress that is due to joining and bending is shown in Fig. 6(b). The direction of the first principal stress also is indicated by arrows. The calculated global stress direction of these tensile stresses in the region of the termination edge correlates with the obtained fracture patterns of the measurements (see Fig. 2) for Mode I failure. The observed fractures always started near the termination edge, where the maximum tensile stresses are calculated.

Each volume element k , before bending at room temperature, shows the principal stresses due to joining ($(\sigma_1, \sigma_2, \sigma_3)_{join,k}$). After exposure to bending, these values change at fracture to $(\sigma_1, \sigma_2, \sigma_3)_{join+bend,k}$ with changed directions. $\sigma_{1,max, join+bend}$ is dominant, the maximum second principal stress $\sigma_{2,max, join+bend}$ is calculated to be $<1\%$ of $\sigma_{1,max, join+bend}$, and $\sigma_{3,max, join+bend}$ is negative. Therefore, the value of $\sigma_{1,max, join+bend}$ is used as $\sigma_{p,i}$ in Fig. 7.

Three sets of parameters $(m_v, \sigma_{OV})_j$ are derived for each measurement series j with the fitted single-distribution function (Eq. (5)), and one set $(\tilde{m}_v, \tilde{\sigma}_{OV})$ is determined for all three series, according to the fitted mean-distribution function (Eq. (6)). These parameters, including the characteristic strength for dominant surface flaws (σ_{OS}), are listed in Table VIII. The maximum tensile stress at which 63.2% of the measured specimens of one series failed is noted as $\sigma_{63.2\%}$.

Statistical separation of the volume and surface effects can be performed only for different stressed-volume:surface-area ratios of the investigated components; however, the nominal volume:surface-area ratio of the three component sizes is within a range of 0.26–0.27 mm. Therefore, fittings of the Weibull parameters for dominant volume flaws and dominant surface flaws (without superposition) are compared as follows.

The confidence intervals for the Weibull parameters of each series are calculated for a confidence level of 90%. Because of the statistical nature of flaw-size distributions and orientations, the “true” (for an infinite number of specimens) distribution function will be within the limits of the 90% confidence intervals. Figure 8 compares the confidence intervals of each series with the results that have been gained by the evaluation of the mean-distribution function $(\tilde{m}_v, \tilde{\sigma}_{OV})$. Table VIII and Fig. 8 both indicate that the

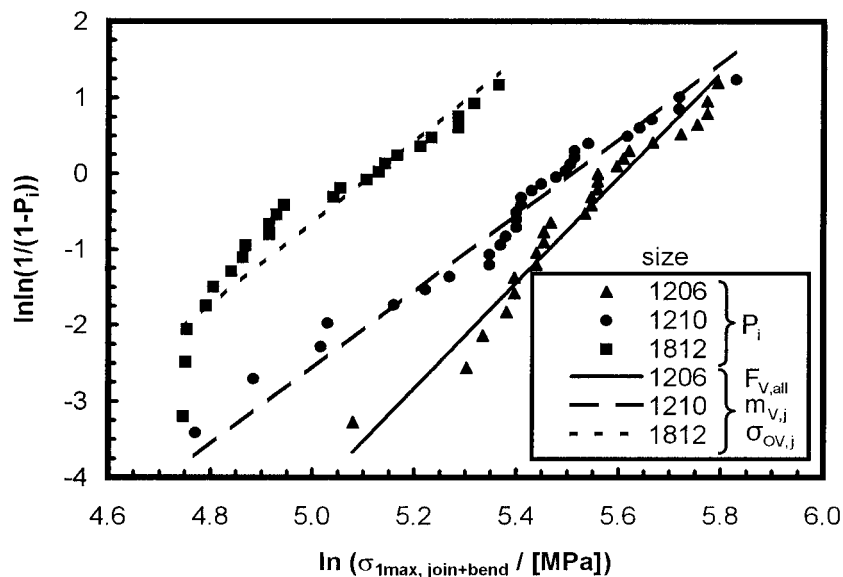


Fig. 7. Weibull plot of single measurements P_i and fitted single-distribution functions $F_{V,all}$ for soldered and bent MLCs.

Table VIII. Weibull Parameters Measured for Single-Distribution and Mean-Distribution Functions

Parameter	Value			Mean distribution
	Single distribution			
	1206	1210	1812	
m_v	6.9	5.0	5.5	6.4
σ_{OV}	112.0 MPa	104.8 MPa	75.9 MPa	105.5 MPa
σ_{OS}	166.4 MPa	154.8 MPa	111.7 MPa	
$\sigma_{63.2\%}$	272.6 MPa	246.6 MPa	167.0 MPa	

results for the 1206 and 1210 sizes obviously are in sufficient accordance with the basic assumptions. The data for the 1812 size is outside the acceptable confidence interval and cannot be brought in-line by considering surface-flaw effects only (Table VIII) or combined volume and surface-area effects. Two additional dominant reasons are under consideration: (i) residual stresses caused by manufacturing are superimposed and can differ from size to size, and (ii) microstructural differences due to material composition and processing lead to different Weibull parameters for each size.

The mean values are used for the investigation of the wave-soldering process, to study the principal impact on the reliability of the 1206 component size. The derived values can be applied to any other load case, assuming dominant volume flaws, an absence of residual stresses, and an isotropic material structure.

(4) Wave-Soldering Process

The simulation of the wave-soldering process is separated into three sections: preheating conditions, soldering, and cooling to room temperature. The time-dependent temperature distribution, the resulting stress distribution due to thermal expansion, and the failure probability due to thermal stresses are calculated for each section.

The first section is used to calculate the initial temperature distribution that is caused by preheating; the preheating temperature (typically 120°C)²¹ is applied to the upper surface of the MLC and the PCB and by cooling the opposite surface of the PCB via convection ($20 \text{ W} \cdot (\text{m}^2 \cdot \text{K})^{-1}$ at 20°C). The preheating is assumed to be a steady-state process, and the temperature distribution is calculated using the above-defined boundary conditions. The second section is used to calculate the time-dependent temperature distribution during actual soldering. This type of analysis is transient. At the moment of solder immersion, boundary conditions that describe the heat transfer between liquid solder and the surfaces that are coming in contact with solder are applied. A difference in heat transfer will exist between the wetted surfaces (component termination) and those which cannot be wetted (ceramic). The heat-transfer coefficient (h) for surfaces that cannot be wetted will be less than that for wetted surfaces. The h value for the nonwetted surfaces is unknown; therefore, all surfaces are simulated with a high h value for ideal (wetted) cross-flow conditions ($h = 150\,000 \text{ W} \cdot (\text{m}^2 \cdot \text{K})^{-1}$ at the solder temperature). Therefore, the calculated heat flow and the failure probability is higher and the temperature increase is faster than expected in practice. The component is kept in place during soldering using a glued center point with negligible influence on the stress profile.

After soldering, the cooldown temperatures are calculated in section three. All the boundary conditions are replaced by conditions for cooling ($h = 20 \text{ W} \cdot (\text{m}^2 \cdot \text{K})^{-1}$ at 20°C), and the analysis is performed transiently. A liquid solder fillet is assumed to adhere between the component and the PCB. The liquid solder influences the thermal calculation, and the mechanical properties are neglected. During cooling, the solder temperature of every time step is checked and each finite element of the solder fillet is turned solid (activating the mechanical properties of solder) when the temperature decreases below the solidus temperature. Stresses (Fig. 6(a)) increase during further cooling to room temperature, because of the different α values of the component and the PCB.

IV. Results and Discussion

The resulting stress distribution for a bending simulation of the three MLC geometries and the Weibull parameters derived from the bending measurements already have been discussed in section III(3). The simulation correlates with the obtained fracture patterns of the measurements for Mode I failure. The crack paths compare very well with the crack paths determined by Prymak and Bergenthal,⁵ which were obtained using a three-point flex test.

Wave soldering is calculated, on principle, for the standard geometry (the 1206 size) with the following base parameters: preheating at 120°C, soldering at 250°C, thirteen inner electrodes, a nickel layer 4 μm thick, and a solder height of 0.87 mm. When immersed in solder, temperature gradients form in the component and stresses are calculated. At the beginning of solder immersion, the stresses initially increase directly under the termination, which is caused by the mismatch of thermal properties. During heating, the increasing stresses become concentrated at the component radii under the termination and ultimately move toward the middle of the component. The direction of the first principal stress moves from perpendicular to the inner electrodes at the beginning of immersion toward an orientation that is parallel to the electrodes before decreasing because of the decreasing temperature gradients. The maximum increase of failure probability versus time (differential failure probability) is observed during the first 30 ms of immersion. A corresponding distribution of the first principal stress is shown in Fig. 9. The maximum tensile stress is ~ 45.9 MPa 15 ms after solder immersion. The primary direction of tensile stresses near high stress levels is indicated by arrows. The simulation of wave soldering leads to stress directions that may explain the types of cracks that were reported by Koripella and DeMatos.⁴ For weak ceramic/metal interfaces at the inner electrodes, delaminations may start in the middle of the component near the termination.

Figure 10 shows the calculated failure probabilities versus load history (preheating, soldering, cooling, and bending) for different preheating temperatures. The bending results are shown for five different bending moments: 0.10, 0.16, 0.22, 0.28, and 0.34 N·m. The failure probability due to thermal shock is in the range of 1×10^{-6} – 5×10^{-3} . Preheating temperatures of 20°, 70°, and 120°C will lead to similar results, because of the course of the dielectric α plot versus temperature, which has a local maximum at 120°C.

The results for the variation of the solder temperature are shown in Fig. 11. The failure probabilities increase monotonously as the solder temperatures increase and are in the range of 1×10^{-7} – 5×10^{-2} . The quoted effects of preheating and soldering temperatures are, principally, consistent with the calculations of Scott and Astfalk.¹² An increase in the failure probability during cooling is observed only for solder temperatures of $<225^\circ\text{C}$.

Because of the preheating and soldering history, bending starts at different failure probability levels and continues its course until fracture occurs. Different solder heights, which are measured from the component bottom to the highest solder location, affect the statistical bending strength of the component (Table IX). The failure probability increases at high levels as the solder heights decrease, which is consistent with the findings of other authors.^{22,23}

The variation of the thickness of the nickel layer (Table X) shows a declining failure probability at low levels with declining thickness of the nickel layer. This trend also was observed using the measurements of Rawal *et al.*²⁴

A minor influence also is observed for the variation of the number of inner electrodes. Almost no differences are observed during wave soldering. A tendency toward declining failure probability with an increasing number of inner electrodes is observed for bending (Table XI), which is in contradiction to the experimental results for the modulus of rupture (MOR) that was measured by Koripella.²⁵ Once again, the inner electrodes are assumed to be one of the driving forces for residual stresses,²⁶ which are neglected in the presented simulation. Furthermore, the MOR (three-point bending) cannot be compared directly with the bending strength of soldered devices, because of the different stress distributions.

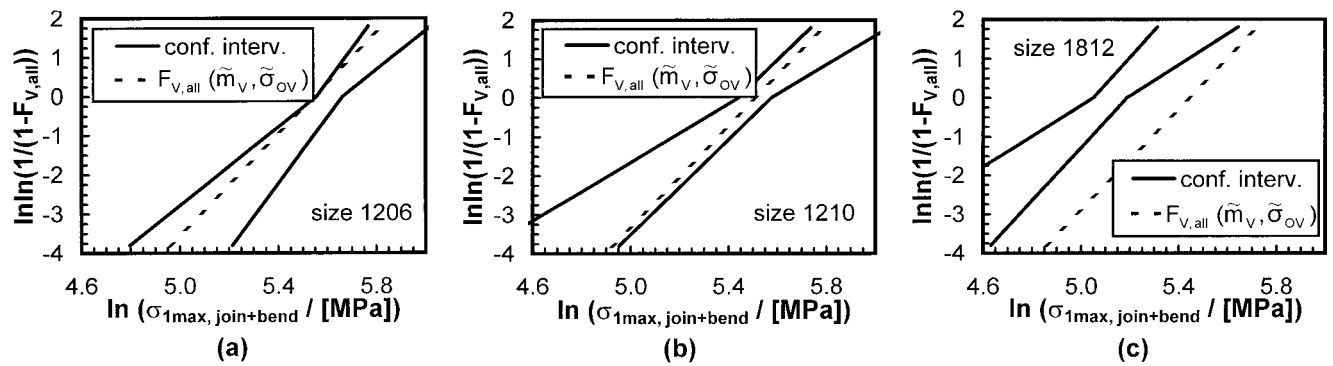


Fig. 8. Single-distribution functions $F_{V,all}$ for each series, calculated by the mean values (\bar{m}_V , $\bar{\sigma}_{OV}$) and 90% confidence intervals for the single measurements (for sizes (a) 1206, (b) 1210, and (c) 1812).

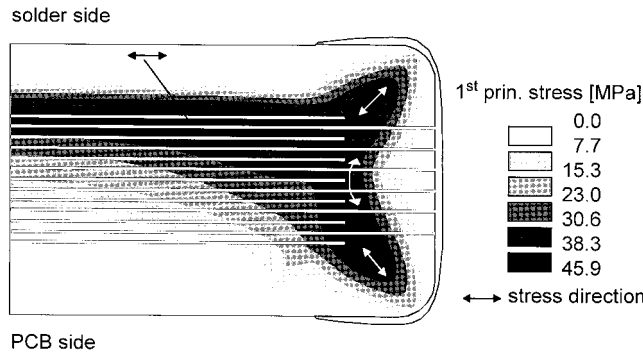


Fig. 9. Distribution of first principal stress in a Type X7R MLC (1206 size) caused by thermal shock 15 ms after solder immersion during a wave-soldering process.

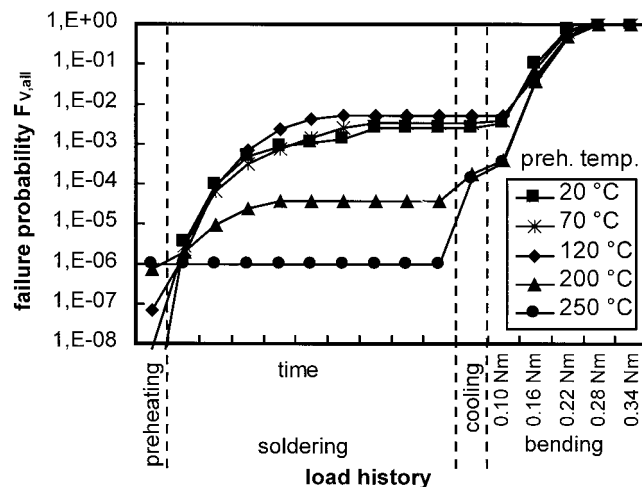


Fig. 10. Failure probability calculated for different preheating temperatures, using the 1206 size with thirteen electrodes, soldered at 250°C.

V. Conclusion

A parameter-based numerical model for simulation of the soldering and bending of multilayer capacitors (MLCs) has been presented. In contrast to most other papers, which have evaluated simulated stresses, the final evaluation in this paper has been conducted based on component failure probability. The failure probability is based on the Weibull theory. For the simplest case of weakest link, an isotropic material structure, a two-parameter approach, and a dominant population of volume flaws have been used. The corresponding Weibull parameters have been derived from analyzing the single-distribution functions (m_V , σ_{OV}), as well as the mean-distribution function (\bar{m}_V , $\bar{\sigma}_{OV}$), which links the three

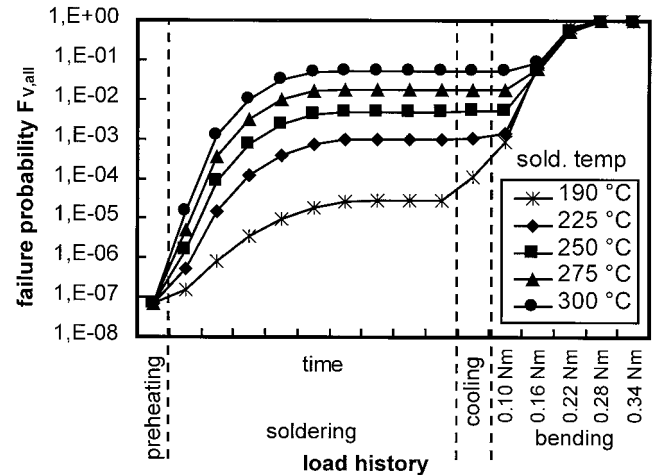


Fig. 11. Failure probability calculated for different soldering temperatures, using the 1206 size with thirteen electrodes, preheated at 120°C.

Table IX. Calculated Failure Probability for Various Solder Heights during Bending (1206 Size)

External bending moment (N·m)	Failure probability for various solder heights (%)			
	0.87 mm	0.68 mm	0.49 mm	0.30 mm
0.10	0.5	0.6	0.8	1.2
0.16	5.6	11.5	21.8	32.2
0.22	56.3	78.6	93.6	98.2
0.28	99.5	>99.9	>99.9	>99.9

individual series. The Weibull parameters for the two smaller sizes—1206 and 1210—show a high conformity with the model assumptions. Comparison of these parameters (m_V , σ_{OV})_{*j=1,2*} to the mean parameters (\bar{m}_V , $\bar{\sigma}_{OV}$) of the largest size (1812) shows that the predicted failure probability is considerably less than the measured value. The 90% confidence interval is not met, which means that some of the basic model assumptions are not valid for the 1812 size, in comparison to the 1206 and 1210 sizes.

The nominal volume:surface-area size proportion resides within a narrow range (0.26–0.27 mm); therefore, in a first approximation, only minor effects are expected, because of the separation or superposition of volume and surface flaws. The main reasons that remain are the superposition of different residual-stress profiles and/or different volume and surface microstructures, which are due to unknown differences in processing.

To study the basic impact on reliability of a MLC (1206 size), the mean Weibull parameters are used. A strong influence on MLC failure probability is observed for different preheating and soldering temperatures, as indicated in the literature. Reducing the height of the solder fillet leads to higher failure probabilities during

Table X. Calculated Failure Probability for Various Thicknesses of the Nickel Layer during Soldering (1206 Size)

Time (ms)	Failure probability for various thicknesses of the nickel layer (%)				
	2 μm	4 μm	6 μm	8 μm	10 μm
0 (preheating)	2.3×10^{-6}	7.0×10^{-6}	3.0×10^{-5}	7.4×10^{-5}	1.6×10^{-4}
1	9.0×10^{-5}	1.6×10^{-4}	2.8×10^{-4}	4.7×10^{-4}	7.7×10^{-4}
7	6.3×10^{-2}	7.1×10^{-2}	8.1×10^{-2}	9.2×10^{-2}	1.0×10^{-1}
85	4.7×10^{-1}	4.9×10^{-1}	5.1×10^{-1}	5.3×10^{-1}	5.5×10^{-1}

Table XI. Calculated Failure Probability for Various Numbers of Electrodes during Bending (1206 Size)

External bending moment (N·m)	Failure probability for various numbers of electrodes (%)			
	5	13	21	29
0.16	6.0	5.6	5.3	5.0
0.22	58.7	56.3	53.9	51.8
0.28	99.6	99.5	99.4	99.2

bending. The number of inner electrodes and the thickness of the nickel layer each exhibit minor influence on the failure probability.

Note that the heat-transfer coefficient (h) during soldering has been set to an extreme upper limit of $h = 150\,000\text{ W}\cdot(\text{m}^2\cdot\text{K})^{-1}$, because the exact value is not yet known. This choice allows study of the effects on failure probability in a wide parameter field; however, the level is beyond realistic expectations. Nevertheless, the modeling approach and the parameter study give strong indications of which dominant technological measures can lead to improved overall service reliability of MLCs.

References

- ¹G. Reindl, "Multilayer Ceramic Capacitors for Automotive Applications: Safe, Rugged and Versatile," *Siemens Compon.*, **30** [5] 20–22 (1995).
- ²P. Ward, "Multilayer Ceramic Capacitor Materials, Process and Reliability"; pp. 51–61 in *Proceedings of the Capacitor and Resistor Technology Symposium, CARTS-EUROPE '89*. ECII Ltd., Crowborough, U.K., 1989.
- ³L. A. Mann, S. P. Gupta, and L. G. Jones, "The Influence of Termination Properties on the Thermal Shock and Thermal Cycle Performance of Surface Mount Multilayer Ceramic Capacitors"; pp. 437–41 in *41st Electronic Components and Technology Conference (ECTC)*. Institute of Electronic and Electrical Engineers (IEEE), Piscataway, NJ, 1991.
- ⁴C. R. Koripella and H. V. DeMatos, "Fractography of Thermal Shock Cracked Multilayer Capacitors"; KEMET Electronics Corp. Bulletin, Rept. No. F-2104A, Greenville, SC, 1990.
- ⁵J. D. Prymak and J. Bergenthal, "Capacitance Monitoring while Flex Testing," *IEEE Trans. Compon., Packag., Manuf. Technol.—Part A*, **CPMT-18** [1] 180–86 (1995).
- ⁶A. A. Wereszczak, K. Breder, M. K. Ferber, R. J. Bridge, L. Riester, and T. P. Kirkland, "Failure Probability Prediction of Dielectric Ceramics in Multilayer Capacitors"; pp. 73–83 in *Ceramic Transactions*, Vol. 97, *Multilayer Electronic Ceramic Devices*. Edited by J.-H. Jean, T. K. Jean, K. M. Nair, and K. Niwa. American Ceramic Society, Westerville, OH, 1999.
- ⁷D. Sander, "Bruchstatistischer FEM-Postprozessor zur Auslegung von Keramischen Bauteilen" (FEM-Postprocessor for Fracture Statistic Analysis of Ceramic Components); Dissertation. RWTH Aachen, Aachen, Germany, 1996.
- ⁸H. R. Maier, M. Magin, W. Kruhöffner, and F. Schmitz, "Reliability Analysis of Active Brazed Ceramic-Metal Joints," *DVS-Ber.*, **184**, 110–13 (1997).
- ⁹Fixed Capacitors for Use in Electronic Equipment. Part 10: Sectional Specification; Fixed Multilayer Ceramic Chip Capacitors"; International standard IEC 384-10, 1989.
- ¹⁰N. N., *ANSYS® Basic Analysis Procedures Guide*, Release 5.3, Swanson Analysis Systems, Inc., Canonsburg, PA, 1996.
- ¹¹W. Duffy, B. L. Cheng, M. Gabbay, and G. Fantozzi, "Anelastic Behavior of Barium-Titanate-Based Ceramic Materials," *Metall. Mater. Trans. A*, **26A**, 1735–39 (1995).
- ¹²G. C. Scott and G. Astfalk, "Thermal Stress in Multilayer Ceramic Capacitors: Numerical Simulation," *IEEE Trans. Compon., Hybrids, Manuf. Technol.*, **CHMT-13** [4] 1135–45 (1990).
- ¹³F. Stelzer, *Physical Property Algorithms—Stoffwertalgorithmen*. Edited by W. Hanle and M. Pollermann. Karl Thieme AG, Munich, Germany, 1984.
- ¹⁴Metals Handbook, 9th Ed., Vol. 2, *Properties and Selection, Non-Ferrous Alloys and Pure Metals*. ASM, Metals Park, OH, 1979.
- ¹⁵Metals Handbook, 10th Ed., Vol. 2, *Properties and Selection, Non-Ferrous Alloys and Special-Purpose Materials*. ASM, Metals Park, OH, 1990.
- ¹⁶M. Cole and T. Caulfield, "Constant Strain Rate Tensile Properties of Various Lead Based Solder Alloys at 0, 50, and 100°C," *Metall. Mater.*, **27** [7] 903–908 (1992).
- ¹⁷A. M. Magomedov, "Density and Elastic Properties of Tin-Lead Solders," *Izv. Akad. Nauk SSSR. Met.*, [5] 197–98 (1990).
- ¹⁸Y. S. Touloukian (ed.), "Thermal Expansion, Metallic Elements and Alloys"; pp. 963–66 in *Thermophysical Properties of Matter*, The TPRC Data Series, Vol. 12. IFI/Plenum, New York, 1975.
- ¹⁹W. Weibull, "A Statistical Theory of the Strength of Materials"; in *The Royal Swedish Institute for Engineering Research*, Proceedings No. 151. Generalstabens Litografiska Anstalts Förlag, Stockholm, Sweden, 1939.
- ²⁰W. Weibull, "A Statistical Distribution Function of Wide Applicability," *J. Appl. Mech.*, **9**, 293–97 (1951).
- ²¹G. Keller, *Oberflächenmontagetechnik* (Surface Mount Technology). Edited by E. G. Leuze. Verlag, Saulgau/Württemberg, Germany, 1995.
- ²²M. J. Cozzolino, "Stress Determination for Surface Mounted Ceramic Capacitors"; pp. 42–52 in *Proceedings of the Capacitor and Resistor Technology Symposium, CARTS '86*. Components Technology Institute, Inc., Huntsville, AL, 1986.
- ²³N. Fujikawa, M. Inagaki, and N. Yokoe, "Simulation and Evaluation of Stresses in Surface Mounted Chip Capacitors"; pp. 292–302 in *Ceramic Transactions*, Vol. 8, *Ceramic Dielectrics: Composition, Processing, and Properties*. Edited by H. C. Ling and M. F. Yan. American Ceramic Society, Westerville, OH, 1990.
- ²⁴B. S. Rawal, R. Ladew, and R. Garcia, "Factors Responsible for Thermal Shock Behavior of Chip Capacitors"; pp. 1–8 in *Technical Information Bulletin*, AVX Corp., Myrtle Beach, SC, 1987.
- ²⁵C. R. Koripella, "Mechanical Behavior of Ceramic Capacitors," *IEEE Trans. Compon., Hybrids, Manuf. Technol.*, **CHMT-14** [4] 718–24 (1991).
- ²⁶G. de With, "Structural Integrity of Ceramic Multilayer Capacitor Materials and Ceramic Multilayer Capacitors," *J. Eur. Ceram. Soc.*, **12**, 323–36 (1993). □